Elucidating the iron-based ionic liquid $[C_4py][FeCl_4]$: structural insights and potential for nonaqueous redox flow batteries

Balischewski, C., Bhattacharyya, B., Bailey, J. J., Place, S. D., Nockemann, P., Kim, J., Wedel, A., Gahlaut, S., Bald, I., Li, W., Garcia, Y., Sperlich, E., Günter, C., Kelling, A., & Taubert, A. (2024). Elucidating the iron-based ionic liquid $[C_4py][FeCl_4]$: structural insights and potential for nonaqueous redox flow batteries. *Advanced Functional Materials*, *34*(12), Article 2311571. https://doi.org/10.1002/adfm.202311571

Published in:
Advanced Functional Materials

ADVANCED FUNCTIONAL MATERIALS
www.afm-journal.de

Elucidating the Iron-Based Ionic Liquid $[C_4py][FeCl_4]$: Structural Insights and Potential for Nonaqueous Redox Flow Batteries

Christian Balischewski, Biswajit Bhattacharyya, Josh J. Bailey, Scott D. Place, Peter Nockemann, Jiyong Kim, Armin Wedel, Shashank Gahlaut, Ilko Bald, Weiyang Li, Yann Garcia, Eric Sperlich, Christina Günter, Alexandra Kelling, and Andreas Taubert**

In this study, a low-melting organic-inorganic crystalline ionic liquid compound, *N*-butyl pyridinium tetrachlorido ferrate (III) is described. The material can easily be synthesized using a one-pot approach in an ionic liquid medium. Single-crystal X-ray diffraction confirms that the basic inorganic block is $[FeCl_4]^-$, which is counterbalanced by an *N*-butyl pyridinium cation. The compound exhibits a melting point of 37.6 °C by differential scanning calorimetry, which is among the lowest values for a pyridinium-based metal-containing ionic liquid. The material shows promising electrochemical behavior at room temperature in both aqueous and nonaqueous solvents, and at elevated temperatures in its pure liquid state. Given its appreciable solubility in both water and acetonitrile, the compound can act as a redox-active species in a supporting electrolyte for redox flow battery applications. These classes of low-melting ionic solids with long-range order and interesting electrochemical applications are potential candidates for a range of green energy storage and harvesting systems.

1. Introduction

Low-melting ionic solids are emerging as an alternative sustainable material for various applications, including energy storage, sensors, and catalysis.[1–6] Above their melting points, these materials can be classified as either inorganic or organic molten salts, depending on their nature. For example, inorganic chloroaluminate molten salts of lithium, sodium, and potassium in various ratios have melting points below 100 °C and are extensively used as solid-state battery electrolytes.[7] Conversely, organic molten salts such as ionic liquids with low melting points, have also been used for similar applications.[8] Upon cooling (and solidification) these materials may be amorphous, crystalline, or liquid crystalline.[9,10] Due to their task-specific designer

C. Balischewski, B. Bhattacharyya, S. Gahlaut, I. Bald, E. Sperlich, A. Kelling, A. Taubert
Institute of Chemistry
University of Potsdam
Karl-Liebknecht-Strasse 24–25, D-14476 Potsdam, Germany
E-mail: biswajit.bhattacharyya@uni-potsdam.de; ataubert@uni-potsdam.de

J. J. Bailey, S. D. Place, P. Nockemann
The QUILL Research Centre
School of Chemistry and Chemical Engineering
Queen's University Belfast
Stranmillis Road, Belfast BT9 5AG, UK

J. Kim, A. Wedel
Functional Materials and Devices
Fraunhofer Institute of Applied Polymer Research (IAP)
Geiselbergstraße 69, D-14476 Potsdam, Germany

W. Li, Y. Garcia
Institute of Condensed Matter and Nanosciences
Molecular Chemistry
Materials and Catalysis (IMCN/MOST)
Université Catholique de Louvain
Place L. Pasteur 1, Louvain-la-Neuve 1348, Belgium

C. Günter
Institute of Geosciences
University of Potsdam
Karl-Liebknecht-Strasse 24–25, D-14476 Potsdam, Germany

The ORCID identification number(s) for the author(s) of this article can be found under https://doi.org/10.1002/adfm.202311571

DOI: 10.1002/adfm.202311571

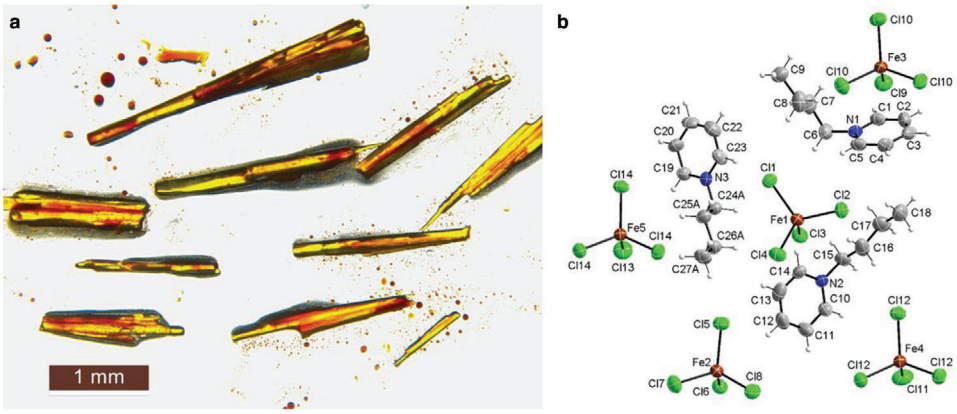

Figure 1. a) Photograph of some liquid crystals of $[C_4py][FeCl_4]$. The crystals look pale yellow but after melting turn into a brown-colored liquid. b) Molecular structure of $[C_4Py][FeCl_4]$ with atomic labels. Displacement ellipsoids are shown at the 50% probability level. Hydrogen bonds are shown in Figure S4 (Supporting Information).

material character and their broad range of electrochemical properties, these materials are also emerging as strong alternatives for solution-based electrochemical applications, such as electrolytes in fuel cells or redox flow batteries. Here the main advantage is a generally higher ion mobility paired with better contact between the electrolyte and the electrode surface.

Over the last decade, there has been remarkable progress in organic-inorganic hybrid materials within material science.[11] More specifically, organic-inorganic metal halides have emerged as one of the most intensively researched and applied materials in energy and optoelectronic applications.[12] In this regard, ionic liquids based on organic–inorganic metal halides are also gaining interest in recent times due to their unique physical and chemical properties, which can be tailored by the choice of metal and ligand components.[13–20]

Here we demonstrate a new iron-based organic-inorganic ionic liquid compound, *N*-butyl pyridinium tetrachlorido ferrate (III), which is synthesized through a single-step procedure in an ionic liquid medium. The material forms needle-shaped crystals. Single crystal X-ray diffraction (XRD) shows that the basic structure is $[FeCl_4]^-$ stabilized by an *N*-butyl pyridinium cation. Differential scanning calorimetry (DSC) and thermo-gravimetric analysis (TGA) show that the material has a remarkably low melting temperature of 37.6 °C and exhibits thermal stability up to 250 °C. In addition to its structural and thermal properties, the material displays interesting electrochemical properties both at room temperature and at temperatures above its melting point. Cyclic voltammetry data show interesting prospects in different solvents and charge–discharge cycling in an H-cell setup illustrates its use as a redox-active species, demonstrating its potential applicability in energy storage.

2. Results and Discussion

N-butyl pyridinium tetrachlorido ferrate (III) ($[C_4py][FeCl_4]$) has been synthesized via a single-step, one-pot synthesis method with high yields (see Experimental for details). In short, the precursors are mixed in isopropanol, heated to reflux, and then allowed to cool to room temperature. The basic reaction scheme of the synthesis is shown in Figure S1 (Supporting Information). **Figure 1a** shows some of the resultant crystals of $[C_4py][FeCl_4]$. The crystals have a distinct pale-yellow color that turns deep brown upon melting. A photograph of the pure liquid state has been provided in the supporting information (Figure S2, Supporting Information) along with its attenuated total reflectance infrared (ATR-IR) spectrum (Figure S3, Supporting Information).

The crystal structure of $[C_4py][FeCl_4]$ was determined by single-crystal XRD analysis, with details found in the Experimental and Supporting Information sections. The compound $[C_4py][FeCl_4]$ crystallizes in the trigonal space group $P31c$ with 18 formula units per unit cell (see Table S1, Supporting Information). There are three $[C_4py]^+$ cations and three $[FeCl_4]^-$ anions in the asymmetric unit. Figure 1b) shows a part of the unit cell, showing that three of the five anions are located on three-fold axes of rotation. The butyl chain of the cation with N3 is disordered in two positions at a ratio of 84:16. In Figure 1b, only part A of the disordered structure is shown. Besides this compound, only two other compounds are known so far with an alkyl pyridinium cation and a $[FeCl_4]^-$ anion (CSD Ref. Code CERJUE and WETPAO).[21] In both compounds, other anions are present in addition to the $[FeCl_4]^-$ anion.

Despite the large number of potential proton acceptors (14 Cl atoms in the asymmetric unit), only a few hydrogen bonds exist between the cations and anions due to the low acidity of the hydrogen atoms in the compound. In total, only four C-H-Cl hydrogen bonds, with an acceptor-proton distance of up to 2.9 Å, are observed (see Figure S4, Supporting Information). As already seen in similar compounds,[13–15] anion-π interactions between the cations and the anions significantly influence the molecular arrangement. Overall, nine of the 12 symmetry-independent Cl atoms form anion-π interactions with an aromatic-Cl distance less than 4.5 Å (Figure S5, Supporting Information). The $[FeCl_4]^-$ anions exhibit tetrahedral geometry. The Cl atoms that are not involved in anion-π interactions, i.e., Cl3, Cl6, and Cl11, form σ-hole interactions with the Fe atoms of neighboring anions. This leads to intermolecular anion chains aligned along the crystallographic *c*-axis (**Figure 2a**).

A 3D geometry analysis using Conquest (CSD) software[22] showed that this intermolecular linkage to anion chains occurs relatively frequently in compounds with tetrahedral $[FeCl_4]^-$

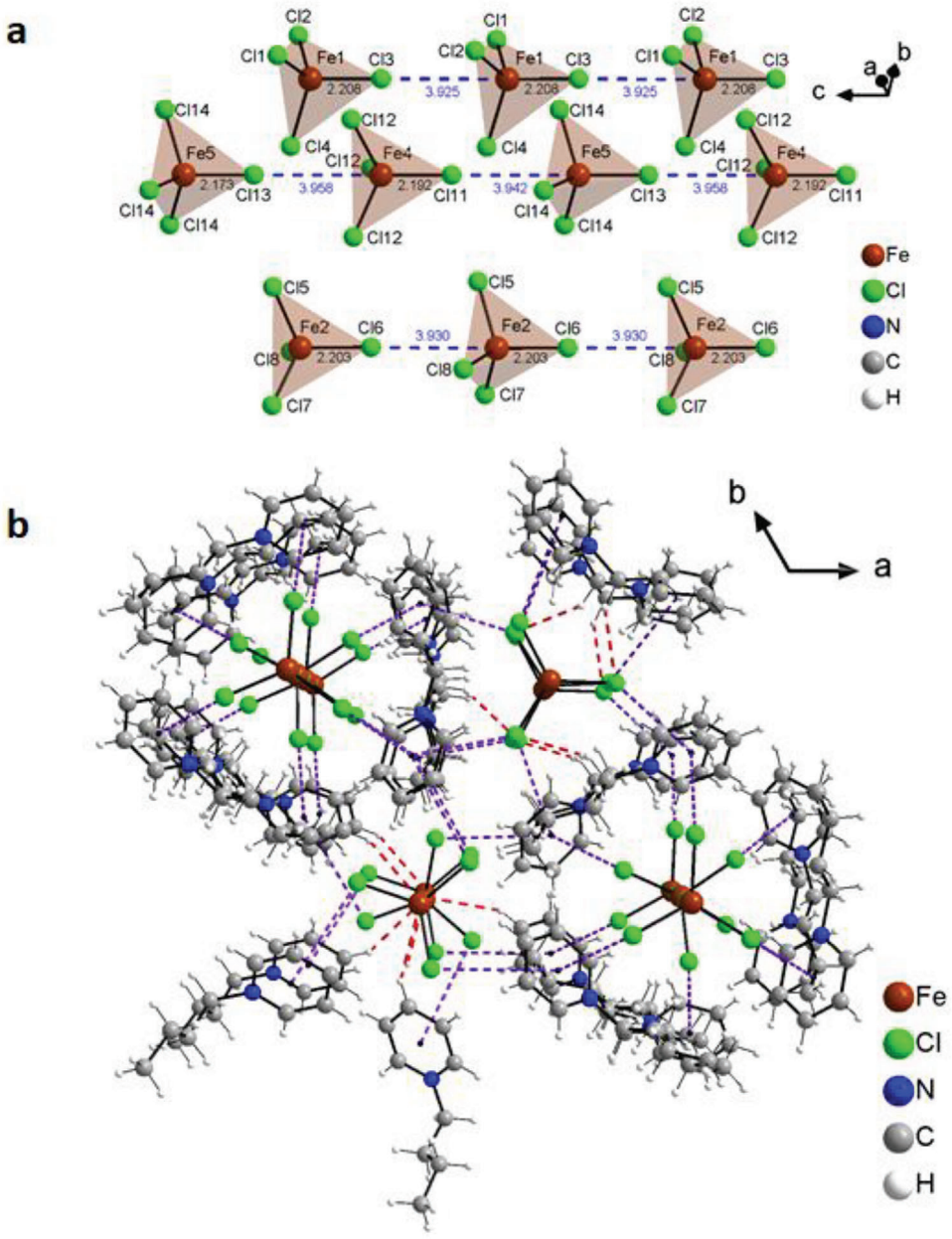

Figure 2. a) Anion-anion chains formed by σ-hole interactions between the Fe atom and the Cl atom of a neighboring anion. b) Arrangement of cations and anions with hydrogen bonds, anion-π interactions, and σ-hole interactions, viewed along the *c*-axis.

anions (see, e.g., CSD Ref. Code CURBIC[23] or DIRKEU01[24]). A Conquest search, using both intermolecular Cl-Fe distance and the Fe-Cl-Fe angle as parameters, revealed a total of 252 compounds (CSD version 5.43 + November 2022 update). The intermolecular distance between a Cl atom of a $[FeCl_4]^-$ anion and the Fe atom of a neighboring anion was determined to be between 2.6 and 5.0 Å and the Fe-Cl-Fe angle between the anions to be between 50° and 180°. Figure S6 (Supporting Information)) shows the heat plot of the results with the intermolecular Cl-Fe distance on the Y axis and the Fe-Cl-Fe angle on the X axis. The region where the values for $[C_4py][FeCl_4]$ are located has been marked with a red dot. The distance between the anions is very short (Cl-Fe distance below 4 Å) and the arrangement of the anion is highly directional (Fe-Cl-Fe angle above 178°). This indicates a strong attractive interaction between the anions. Figure 2b shows the packing of $[C_4py][FeCl_4]$ including the hydrogen bonding (red dashed lines), the anion-π interactions (purple dashed lines), and the σ-hole interactions blue dashed lines, along the c-axis). Both parts of Figure 2 show that the tetrahedral structures of the anions are not identically placed but rather alternating in their alignment as a result of minimizing the repulsive interactions. Interestingly, the compound shows an absence of strong Coulomb interactions between the ions and strong intermolecular interactions, such as N-H-Cl bonds, which probably

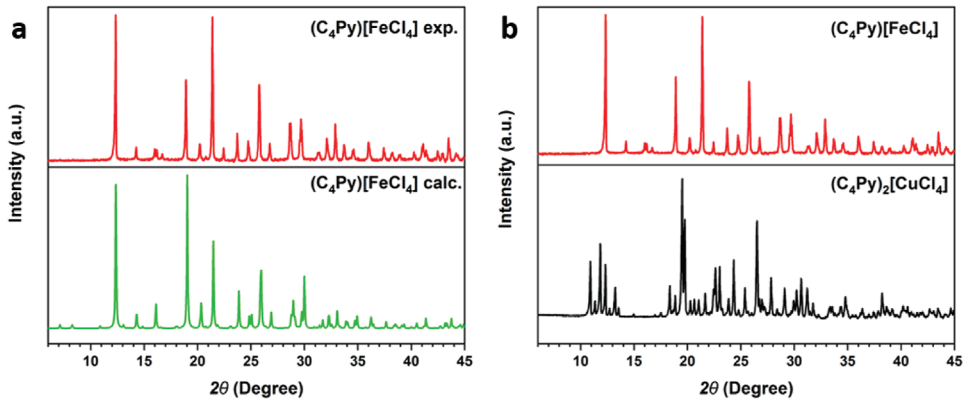

Figure 3. a) Powder XRD pattern of $[C_4py][FeCl_4]$ where the red line is the experimentally obtained pattern and the green line is the simulated pattern. The simulated pattern is calculated from the single-crystal structure. b) Comparative powder XRD data of $[C_4py][FeCl_4]$ (red line) and $[C_4py]_2[CuCl_4]$ (black line) at the lower angles of two theta.

explain the low melting temperature. Figures S7–S9 (Supporting Information) show the cell view along the three spatial directions.

Furthermore, the Fe-Cl bond lengths are ≈2.2 Å, as shown in Figure 2a. This is in agreement with a previous study on tetrachlorido ferrate compounds, reporting average bond lengths of 2.19 Å for the $[FeCl_4]^-$ anion and 2.29 Å for the $[FeCl_4]^{2-}$ anion, with the Fe(II) variant showing a flattened tetrahedral structure.[25–30] The single crystal analysis resulted in a cation: anion ratio of 1:1. Consequently, as the *N*-butylpyridinium cation can only be charged +1, the oxidation state of iron has to be +3. In combination with the average bond length, which is typical for Fe^{III}, the analysis confirms that the compound contains Fe(III) instead of Fe(II).

Figure 3a shows the powder XRD pattern of $[C_4py][FeCl_4]$. The experimental data (green line) corresponds well to the simulated powder XRD pattern (red line) based on the single crystal analysis. This shows that the bulk material does not include significant amounts of side products or exhibit degradation. However, the experimental powder XRD data is quite different from other reported tetrachlorido compounds, as shown in Figure 3b. Although both compounds share a similar tetrahedral environment, this implies a difference in the central metal oxidation state of iron. In order to further confirm the oxidation state, Mössbauer spectroscopy was performed for $[C_4py][FeCl_4]$, shown in Figure S10 (Supporting Information). As seen in Figure S11 (Supporting Information), no signal could be observed after 3 weeks of accumulation. Given that enough iron centers were present in the material, the absence of signal is attributed to a soft crystal lattice, leading to a low recoilless fraction at room temperature. As a result, X-ray photoelectron spectroscopy (XPS) was carried out to better identify the oxidation state.

High-resolution XPS analysis was performed to investigate the chemical state of Fe present in $[C_4py][FeCl_4]$ (**Figure 4**), where the binding energy of C-C bond (aliphatic chain of $[C_4py]^+$, Figure S12a, Supporting Information) was charge-corrected by setting it as equal to 285.0 eV. The Fe 2p data of $[C_4py][FeCl_4]$ requires two components to be fitted, and its primary component, peaking at 711.73 eV, shows a slightly higher binding energy than that of $FeCl_3$ (711.3 eV).[31] Basically, in the binding energy shift of

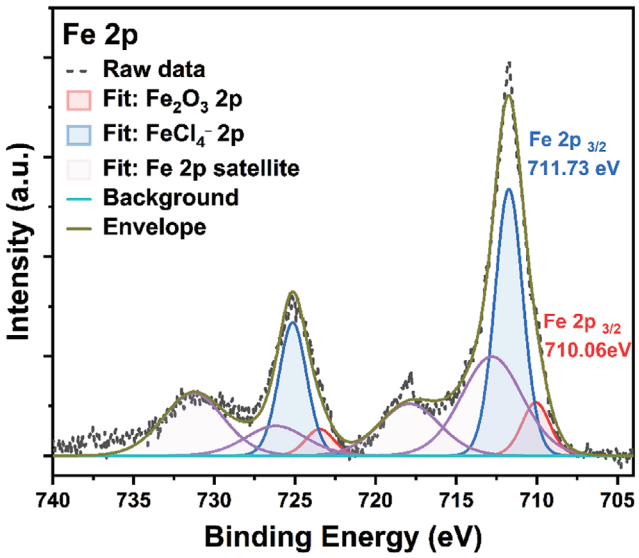

Figure 4. High-resolution XPS spectrum of Fe 2p in $[C_4Py][FeCl_4]$.

XPS, the more chemical bonds with electronegative atoms (e.g., anions) located in the chemical structure, the greater the positive XPS chemical shift.[32,33] In other words, when $FeCl_3$ forms the $[FeCl_4]^-$ anion of $[C_4py][FeCl_4]$ (Figure S12b, Supporting Information), an additional Cl anion can induce greater cationic characteristics in the central Fe cation, which alludes to causing the Fe 2p of $[C_4py][FeCl_4]$ with higher binding energy. On the other hand, the minor component, peaking at 710.06 eV, corresponds to the binding energy in Fe_2O_3, and its O 1s peak was simultaneously detected (Figure S12c, (Supporting Information), which means the surface of $[C_4py][FeCl_4]$ was partially oxidized in air during and/or after synthesis.[34] Also, as there is only one N signal, which can be assigned to cationic nitrogen at 422.55 eV (Figure S12d, Supporting Information); this strongly supports that both the $[C_4py]^+$ cation and the $[FeCl_4]^-$ anion exhibit ionic bonding characteristics.[35–37]

The anisotropic crystal structure of $[C_4py][FeCl_4]$ leads to interesting thermal properties. **Figure 5** shows the corresponding

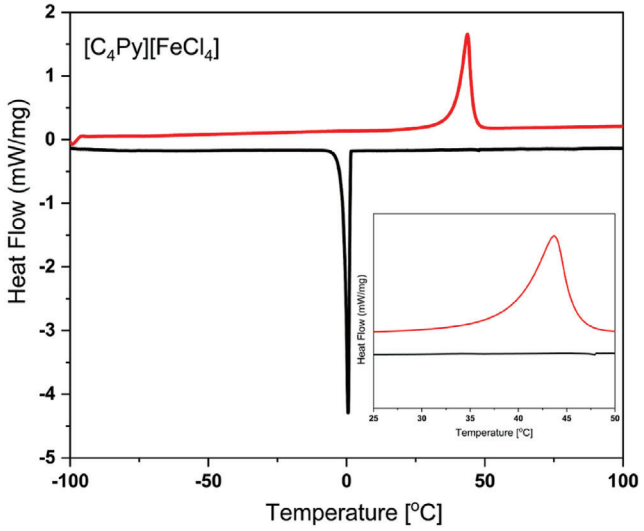

Figure 5. DSC data of $[C_4py][FeCl_4]$ where the red line is the second heating cycle and the black line is the second cooling cycle of the measurements.

DSC data. The red and black lines represent the heating and cooling cycle, respectively. $[C_4py][FeCl_4]$ does not show any glass transition. The sharp peak at 0 °C indicates a cold crystallization (T_c) and the intense signal with a slightly broader peak at 37.6 °C is the melting transition (T_m). Interestingly, the compound has a much lower melting point than the parent compound *N*-butyl pyridinium chloride and one of the lowest melting points for a metal-containing ionic liquid structure.[13–20] The decrease in melting temperature is probably due to the anisotropic tetrahedral arrangement of the $[FeCl_4]^-$ moiety and due to the lack of anion-π interactions and hydrogen bonds in the long-range order of the material. TGA of the sample shows the compound is stable up to 250 °C without any degradation, as shown in Figure S13 (Supporting Information).[38]

Figure 6a shows the solid-state UV–vis spectrum of $[C_4py][FeCl_4]$ at room temperature. The spectrum shows a strong absorption band in the 3 eV region, which is the typical optical absorption for $[FeCl_4]^-$ in a tetrahedral geometry.[39] Other small peaks at 2.75 eV (450 nm) and 2.35 eV (530 nm) are the corresponding absorptions of $^1A_6$ to $^2E(a)$ and $^1A_6$ to $^2E(b)$ states of the *N*-butyl pyridinium ligand. Figure 6b shows the Raman spectrum of $[C_4py][FeCl_4]$. The vibrations for the $[FeCl_4]^-$ complex anion with Td symmetry can clearly be observed. The value of 330 cm^{-1} is ascribed mainly to the A1 mode which is very similar to all reported tetrachlorido ferrate anions.[38,40–42] It is also reported as a totally symmetric stretch of $[FeCl_4]^-$. The peak at 420 cm^{-1} would imply that there could be a laser-induced dimerization form such as $[Fe_2Cl_7]^-$.[43] However, no corresponding peak was observed at 370 cm^{-1}.

Iron-based materials are gaining increasing attention for their potential in energy storage systems. This is mainly due to their generally safe character and the abundance of iron, which results in cost-effectiveness. In 2017, Valvo et al.[44] used a nanomaterial based on lithium and iron as an electrode in a rechargeable lithium-ion battery, creating a more environmentally friendly and safer system due to the exclusion of fluorine, while maintaining the performance of the conventional $LiFePO_4$ system. More appealing still is the use of Fe-based materials as electrolytes. The first rechargeable Fe-Fe-batteries using IL-based compounds as electrolytes are emerging as promising alternatives to standard Li-based devices. Here, the movement of the Fe^{3+} ion between the electrodes during the charge-discharge process is the proposed charge-carrying mechanism of the battery.[45]

A specific battery type that has gathered increasing interest in the last decade, particularly for large-scale, long-duration storage, is the redox flow battery (RFB). RFBs are attractive due to their long lifecycles, customizability, and scalability.[46–48] Typically, this battery type employs two different electrolytes, at the positive electrode (the posolyte) and at the negative electrode (the negolyte). The electrolytes store energy while redox reactions take place at the electrodes, with a membrane separating the two to prevent mixing and short-circuiting, as well as to facilitate the transfer of charge-carrying ions.[46] Although vanadium-based RFBs are now semi-commercialized, the high costs and price volatility of vanadium have hindered market adoption. Iron-based RFBs are attracting increasing attention as they present a more cost-efficient approach.[49,50] The all-iron hybrid battery system ($Fe^{3+/2+}|Fe^{2+/0}$), introduced in 1981 by Hruska and Savinell,[51] demonstrated the potential for such a system, but given that the negative electrode involves plating or dissolving solid metal iron, the capacity of the system and attainable power of the cell are no longer decoupled. This type of battery also suffers from dendrite formation and hydrogen evolution.[48,51] Since then, various organic molecules have been investigated as ligands in iron complexes for their electrochemical properties,[52–54] and various iron-based RFBs based on these complexes have been studied, including: $Fe^{3+/2+}|Br_2/Br^-$,[55] $Fe^{3+/2+}|Co^{3+/2+}$,[56–59] and all-soluble, all-iron systems ($Fe^{3+/2+}|Fe^{2+/1+}$) and ($Fe^{3+/2+}|Fe^{3+/2+}$).[60–67] Despite competitive efficiencies with the incumbent vanadium system, many of the systems involve strongly alkaline systems, and recent efforts have focused on moving to near-neutral systems to minimize pH-dependent stability issues and lessen the demands on suitable cell materials.[68]

In this context, $[C_4py][FeCl_4]$ was investigated for its electrochemical suitability as a redox-active species. A unique advantage of this iron-based ionic liquid over traditional aqueous metal complexes is the absence of an added base and a potentially simplified system.[69] Moreover, $[C_4py][FeCl_4]$, like many other pyridine-based ionic liquids,[13–15,70] has an appreciable solubility in both aqueous (e.g., 0.5 M in H_2O) and non-aqueous (e.g., 0.3 M in MeCN) solvents, allowing for analysis of its redox behavior in the context of aqueous or nonaqueous RFBs. Cyclic voltammetry (CV) was performed in the pure liquid state at elevated temperatures as well as for $[C_4py][FeCl_4]$ dissolved in water, and $[C_4py][FeCl_4]$ dissolved in MeCN, to fully probe its redox behavior. The cyclic voltammogram for the pure liquid state (at 60°C) is shown in Figure S14 (Supporting Information), demonstrating reproducible oxidative and reductive peaks but displaying a large peak-to-peak separation (>1 V at 50 mV s^{-1}) due to low ionic conductivity, resulting from high viscosity and no supporting electrolyte. Further cyclic voltammetry data of the pure IL is presented in Table S2 (Supporting Information). Its redox potential, +0.275 V (vs AgCl/Ag), is similar to that measured on a Pt electrode for $[C_1C_2im][FeCl_4]$, +0.207 V (vs AgCl/Ag).[71] Given

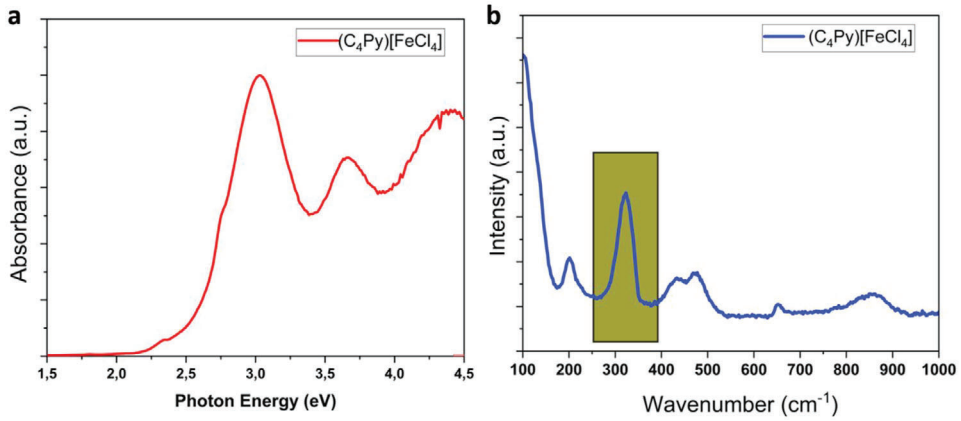

Figure 6. a) Solid-state absorption spectra of $[C_4py][FeCl_4]$ at room temperature. The data have been acquired through UV reflectance measurements. b) Raman spectrum of $[C_4py][FeCl_4]$ with the A1 mode highlighted in gold.

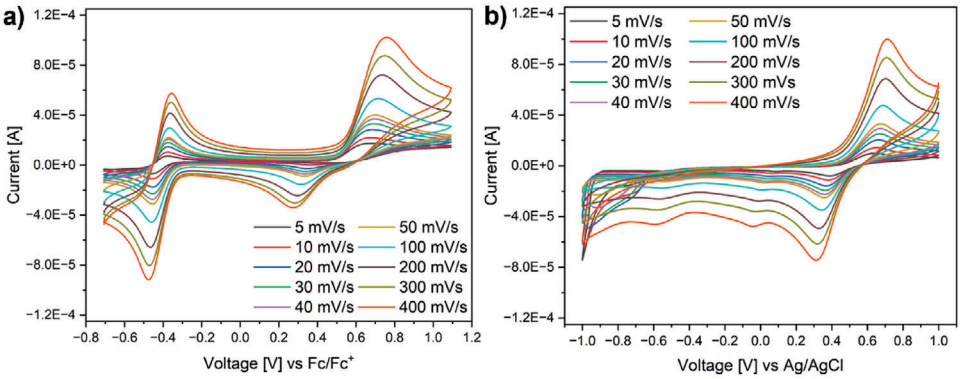

Figure 7. a) Cyclic voltammograms of $[C_4py][FeCl_4]$ in a solution of 100 mM TBAP (tetrabutylammonium perchlorate) in MeCN; b) Cyclic voltammograms of $[C_4py][FeCl_4]$ in a solution of 1000 mM KNO_3 in H_2O.

the higher viscosity associated with the pure metal ionic liquid, and the inherent pumping losses associated with circulating this around an RFB cell, the focus here is the redox behavior when dissolved in a solvent medium, dramatically reducing its viscosity.

Figure 7 shows the cyclic voltammograms of $[C_4py][FeCl_4]$ under dissolved conditions; MeCN (Figure 7a) and water (Figure 7b) were used as solvents, as MeCN is a standard solvent for non-aqueous RFBs,[72,73] while water is naturally the solvent of aqueous RFBs.

Clearly, two redox processes are visible in the non-aqueous case (Figure 6a); a pseudo-reversible redox process at −0.415 V (vs Fc^+/Fc) and an irreversible process at +0.516 V (vs Fc^+/Fc). For the irreversible process, at a given scan rate, the oxidative peak is larger than the respective reductive peak, with the ratio of peak oxidative current (I_{ox}) to the peak reductive current (I_{red}) increasing with decreasing scan rate. This might represent the oxidation of chloride to elemental chlorine, whereby the latter diffuses away readily, and at the lowest scan rate (5 mV/s), no chlorine would be present to be reduced such that the reductive peak is absent. The pseudo-reversible redox process at −0.415 V (vs Fc^+/Fc) is assigned to the $[Fe(III)Cl_4]^-/[Fe(II)Cl_4]^{2-}$ redox process. A negative redox potential versus Fc^+/Fc has been observed previously where the redox potential of $[Fe(III)Cl_4]^-/[Fe(II)Cl_4]^{2-}$ in an ionic liquid medium was determined at a Pt electrode to be −0.220 V (vs Fc^+/Fc).[74] In this case, the redox active species was derived from dissolving $FeCl_3$ and 1-*N*-butyl-1-methylpyrrolidinium chloride ($[C_1C_4pyrr][Cl]$) in 1-*N*-butyl-1-methylpyrrolidinium bis(trifluoromethylsulfonyl)imide ($[C_1C_4pyrr][TFSI]$). Although a direct comparison is difficult as the solvent environments are different, it may be that the $[C_4py]^+$ cation yields a lower redox potential compared to when $[C_1C_4pyrr]^+$ is the counter-cation. This redox process has a peak-to-peak separation, ΔE_p, of 78 mV at 5 mV s^{-1}. As this value is close to the reversible value of 59 mV, this likely indicates an outer-sphere electron transfer wherein no bonds are made or broken.[73,75,76] Support for attributing these processes to the peaks observed is given by the fact that oxidative currents for the irreversible process at +0.516 V (vs Fc^+/Fc) are approximately two times greater than those at −0.415 V (vs Fc^+/Fc), which might indicate two-electron oxidation of chloride to chlorine however, this is only a hypothesis as we do not know the exact reaction mechanisms and kinetics involved at this stage. Consequently, the irreversible redox process occurring at higher potentials has to be further investigated to be identified conclusively. Nonetheless, it is likely that the reversible redox process is a one-electron

transfer at the iron center, as the potential is similar to that reported in the literature. Given that the redox process at negative potentials is pseudo-reversible, a Randles-Sevcik analysis can be applied to estimate the diffusion coefficients of the oxidized and reduced species, as per Equation (1).[73,77]

$$i_p = 2.69 \times 10^5 n^{3/2} AC\sqrt{Dv} \quad (1)$$

Where i_p is the peak current in A, n is the number of electrons in the redox process, A is the electrode area in cm^2, C is the concentration in mol cm^{-3}, D is the diffusion coefficient in $cm^2\ s^{-1}$, and v is the scan rate in V s^{-1}.

Taking the peak oxidative and reductive currents across the 50–400 mV s^{-1} range, the diffusion coefficients of the oxidized and reduced species are estimated to be 8.5×10^{-7} and 2.5×10^{-6} $cm^2\ s^{-1}$, respectively (Figure S15, Supporting Information). These values are on average an order of magnitude greater than those measured for $[Fe(III)Cl_4]^-/[Fe(II)Cl_4]^{2-}$ in an ionic liquid ($[C_1C_4pyrr][TFSI]$) medium ($\approx 1 \times 10^{-7}$ $cm^2\ s^{-1}$) which may result from the lower viscosity in MeCN versus the ionic liquid.[74] Cyclic voltammograms for ferrocene and TBAP in MeCN and solely TBAP in MeCN are included for completeness in Figure S16a,b, (Supporting Information) respectively.

In the aqueous case, there is a couple at +0.514 V (vs AgCl/Ag) which is much less electrochemically reversible than the non-aqueous case, with an ΔE_p of 248 mV at 5 mV s^{-1}. In addition to this, two minor reductive peaks are visible at ≈0 and −0.575 V (vs AgCl/Ag), which might suggest that in H_2O, $[C_4py]^+$ is more susceptible to irreversible reduction. Nevertheless, as the CV was performed in the open air, dissolved gases may also give rise to the small additional peaks observed.[73] Additional CV data for both aqueous and non-aqueous measurements are shown in Table S3 (Supporting Information). Given the greater solubility of $[C_4py][FeCl_4]$ in water, further investigation into limiting these processes (or removing impurities) responsible for these peaks is warranted but beyond the scope of this work.

Given the pseudo-reversibility of the non-aqueous system and the negative potential of the IL (vs Fc^+/Fc), $[C_4py][FeCl_4]$ dissolved in MeCN was paired with a highly reversible redox couple, $TEMPO^+$/TEMPO (2,2,6,6-tetramethylpiperidine-1-oxyl), which is also soluble in MeCN and has a positive potential (≈+0.2 vs Fc^+/Fc).[78] Charge-discharge cycling was performed with the H-cell set-up described in the Experimental and shown in Figure S17 (Supporting Information). **Figure 8** shows the potential and current as a function of time during charge-discharge cycling at a constant current of +/-4 mA (≈+/-8 mA cm^{-2} based on geometric active area). We do acknowledge the rather large voltage drop in the initial H-cell tests. This is rather common in H-cell setups as there is a comparatively large distance between the electrodes. Additionally, this is further explained by the absence of a supporting electrolyte, which was not used to ensure that the occurring redox processes are strictly in the active species of interest.

Cyclic voltammograms of the negolyte ($[C_4py][FeCl_4]$) and posolyte (TEMPO) in the full cell set-up are shown in Figure S18a,b, (Supporting Information)respectively, giving rise to an open-circuit voltage (OCV) of 0.621 V. In the charge-discharge cycling, 0.1 M solutions without supporting electrolytes were investigated, in line with many recent studies of non-aqueous RFB systems.[45,79–81] This lowers the impact of mass transport polarisation, particularly significant in a static H-cell set-up, but gives rise to substantial ohmic polarisation given the limited ionic conductivity of the system. Nonetheless, charge-discharge behavior for this system is demonstrated for the first time (Figure 8), with average coulombic and voltage, and efficiencies of 40% and 18%, respectively. Although these efficiencies are relatively low, this is an unoptimized cell and substantial improvements will be made in future work. It is important to highlight that the here presented unoptimized cell is the first iteration of a system that can be improved in many ways, such as cell geometry, electrode, and membrane choice, or selection of corresponding posolyte. Therefore, this setup presents the first promising step in an ongoing longer development process with multiple optimization options. The fact that the maximum charge time of 270 s (first cycle) at 4 mA constitutes 0.3 mAh which represents ≈1% of the available redox active materials is a further indication that cell optimization is needed. Among others, the high overpotentials may lead to unwanted side reactions but the charge-discharge data clearly demonstrates a proof-of-concept.

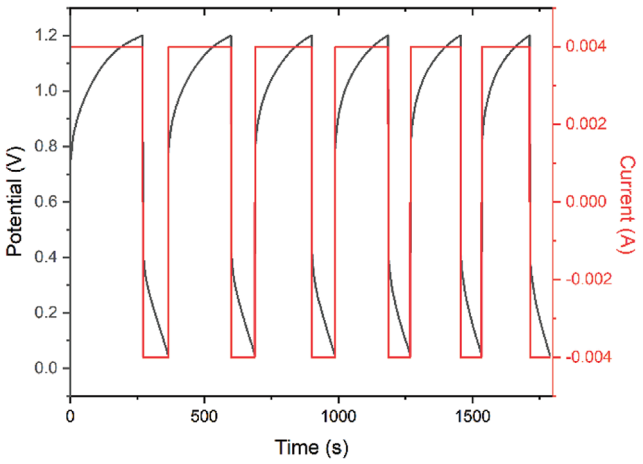

Figure 8. Plot of galvanostatic charge-discharge cycling data of 0.1 M $[C_4py][FeCl_4]$ in MeCN solution as negolyte and a 0.1 M TEMPO in MeCN solution as posolyte in an H-cell set-up.

3. Conclusion

This article presents a promising iron-based ionic liquid compound, $[C_4py][FeCl_4]$, showcasing its potential for energy storage applications. The structure of the metal-containing ionic liquid is elucidated through single-crystal and powder X-ray diffraction providing the first crystal structure for this compound. Along with its thermal and optical properties, the oxidation state of the Fe species in the tetrachloridoferrate anion has been investigated through Raman spectroscopy, crystal structure analysis, and X-ray photoelectron spectroscopy. Additionally, the solubility and redox activity of the compound in both aqueous and non-aqueous solvents are explored, highlighting its versatility. The electrochemical behavior of the Fe-based MIL is studied using cyclic voltammetry in the two most common flow battery solvents (MeCN and water) and charge-discharge cycling in an

H-cell setup demonstrates its potential as a redox active species for non-aqueous RFBs. The findings of this study pave the way for further exploration and optimisation of this compound, contributing to the development of more cost-efficient and environmentally friendly energy storage systems.

4. Experimental Section

Chemicals: *N*-butyl pyridinium chloride (Merck, ≥98.0 %), Anhydrous Iron (II) Chloride (Alfa Aesar, ≥98.0 %), Propan-2-ol (VWR, ≥99 %), Magnesium sulfate AnalaR NORMAPUR (VWR, ≥98.0 %,), Acetonitrile (VWR, ≥99.9 %) and 2,2,6,6-tetramethylpiperidine-1-oxyl, also known as TEMPO (TCI, ≥98.0 %) were used as received.

Synthesis: $[C_4py][FeCl_3]$ has been synthesized in a single-step method with slight modifications from the other reported transition metal-based halidomellate compound. 1000 mg (5.8 mmol) N-butyl pyridinium chloride (C_4pyCl) and anhydrous $FeCl_2$ salt with the equimolar ratio (770.6 mg of $FeCl_2$) were dissolved in 10 mL Propan-2-ol. The reaction was held at 110 °C for 180 min under reflux conditions. Then the reaction mixture was cooled and kept at room temperature overnight. Rotary evaporation was used to remove the solvent and additional water, and the compounds were then dried under vacuum (10^{-3} bar) for 6 h. The final compound was directly used for further analysis without purification. The absolute chemical yield of the reactions was close to 90%. The synthesis was repeated multiple times to show reproducibility.

The compound $[C_4py][FeCl_4]$ was crystalized using the following steps: 1) saturated solution of $[C_4py][FeCl_4]$ was prepared using a mixture of ethanol and propan-2-ol. Then it was kept in a cold place. After 8 weeks, crystals were formed. 2) crystals were collected directly from the bulk material and used for single-crystal analysis.

Infrared Spectroscopy: A NICOLET iS5 by Thermo Scientific was used for the IR measurements alongside an ID7 ATR-attachment with a diamond crystal. The samples were measured using the ATR mode between 4000 and 400 cm^{-1} with a resolution of 4 cm^{-1} and 64 scans. The sample was measured as a powder.

Thermogravimetric Analysis: Thermogravimetric analysis (TGA) was carried out on a Mettler Toledo TGA 2 Thermogravimetric Analyzer (temperature range: 25 to 1000 °C, mass resolution: 0.1 mg) at a heating rate of 10 K min^{-1} under nitrogen flow in aluminum crucibles.

Single Crystal Structure Analysis: A suitable single crystal of the compound was selected using a Leica M205C light microscope and was separated with oil. The X-ray diffraction experiment was carried out on a Stoe Stadivari with monochromated Mo-Kα radiation (λ = 0.71073 Å) and a Pilatus 200 K detector. The measurement was done at 210 K using an Oxford Cryosteam cooling device. The data were corrected using the program X-Area and the structure was solved by direct methods and refined against F^2 on all data by full-matrix least-squares using the SHELX suite of programs.[82,83] The crystal structure was visualized with Diamond.[84] The crystallographic data (CCDC-2244818) can be obtained free of charge from the Cambridge Crystallographic Data Centre, http://www.ccdc.cam.ac.uk.

Powder X-ray Diffraction: X-ray powder diffraction data were collected on a PANalytical Empyrean powder X-ray diffractometer in a Bragg–Brentano geometry using Cu K_α radiation (λ = 1.5419 Å). It was equipped with a programmable divergence, an anti-scatter slit, and a large Ni-beta filter. The PIXcel1D detector was set to continuous mode with an active length of 3.0061°. Scans were run in a 2θ range of 4–70° with a step size of 0.0131° operating at 40 kV and 40 mA. A sample rotation time of 1 s was used.

Differential Scanning Calorimetry: DSC measurements were done using a Netzsch DSC 214 Polyma at 5 or 10 K min^{-1} under nitrogen. Each run consisted of three heating-cooling cycles.

UV/Vis-Spectroscopy: UV/Vis measurements were conducted using a Perkin-Elmer Lambda 950 with the solid material attachment Harrick Scientific Products Inc. Praying MantisTM . During the experiments $MgSO_4$ AnalaR NORMAPUR by VWR was used as a background material. The measuring range was λ = 850–250 nm with a resolution of 2 nm. The Kubelka–Munk equation was used for the analysis of the UV/Vis data.

$$\frac{K}{S} = \frac{(1-R)^2}{2R} \tag{2}$$

K = absorption coefficient, S = scattering coefficient, R = reflectance.

Based on the UV/Vis analysis the optical band gaps were graphically analysed using the Tauc plot. The plots were then fitted via Origin.

$$(\alpha h\nu)^{1/n} = A\left(h\nu - E_g\right) \tag{3}$$

h = Planck's constant,ν = photon's frequency, α = absorption coefficient, E_g = band gap, A = proportionality constant with the following values for n: n = 1/2 for direct allowed transitions, n = 3/2 for direct forbidden transitions, n = 2 for indirect allowed transitions, n = 3 for indirect forbidden transitions.

Raman Spectroscopy: Raman spectra of $[C_4Py][FeCl_4]$ were measured on the HORIBA LabRAM HR Evolution Raman spectrometer at 532 nm laser excitation. The sample was taken on a cleaned glass slide under a 10× magnification objective with 0.25 numerical aperture (NA). Integration time was kept at 2 s for five number of accumulations.

Mössbauer Spectroscopy: ^{57}Fe Mössbauer spectra were recorded at room temperature in transmission geometry with a constant acceleration mode conventional Wissel spectrometer equipped with a Cyclotron Ltd high quality 50 mCi ^{57}Co(Rh) source and a Reuter Stokes proportional counter. The $[C_4py][FeCl_4]$ solid sample was refrigerated and stored in a cold room prior to measurement. 232 mg of sample was transferred to a plexiglass circular sample holder and mounted on the spectrometer. Calibration was preliminary performed with a reference standard (α-Fe) at room temperature.

X-Ray Photoelectron Spectroscopy: X-ray photoelectron spectroscopy (XPS) spectra were obtained with an Axis Supra+ (Kratos Analytical, UK), where a monochromatised Al Kα radiation was used for an excitation source (15 kV, typical 20 mA). CasaXPS software was used for data processing and interpretation, in which XPS signals were fitted using GL (30) lineshapes that combined the Gaussian (70%) and Lorentzian (30%) line shapes.[31] This line shape has been applied equally in the fitting of XPS spectra.

Cyclic Voltammetry: Aqueous CV was performed on solution containing 5 mM $[C_4py][FeCl_4]$, 1000 mM KNO_3 dissolved in H_2O, using a three-electrode set-up consisting of a glassy carbon (⌀ = 3 mm) working electrode (WE), Pt mesh counter electrode (CE) and a AgCl/Ag reference electrode (RE) in a 3 M KCl environment. The WE was polished sequentially using 1.0 and 0.3 µm alumina on polishing pads (MicroCloth, Buehler) before use. The potential was scanned using a potentiostat (PGSTAT302N, Autolab) from +1.0 V to −1.0 V (vs AgCl/Ag), set at scan rates of 5, 10, 20, 30, 40, 50, 100, 200, 300, and 400 mV s^{-1} in proprietary software (Nova 2, Autolab).

Non-aqueous CV was performed on a solution containing 5 mM $[C_4py][FeCl_4]$, 100 mM tetrabutylammonium perchlorate (TBAP) dissolved in MeCN, using a 3-electrode set-up consisting of a glassy carbon (⌀ = 3 mm) WE, Pt mesh CE, and a Ag^+/Ag RE calibrated against a ferrocene standard in the same solution. A blank CV of solely 100 mM TBAP in MeCN solution was also run for confirmation of the electrochemical stability window of this supporting electrolyte.

Galvanostatic Charge Discharge Setup: An H-cell setup was used to explore the charge-discharge behavior of $[C_4py][FeCl_4]$ in a nonaqueous environment. A Nafion cation exchange membrane (N117, Chemours, US) with 180 µm thickness, was soaked in a 100 mM TBAP in MeCN solution for 4 h at room temperature. The soaked membrane was sandwiched between two glass half-cell vessels as shown in Figure S13 (Supporting Information), using laser-cut sponge rubber gaskets (ethylene propylene diene monomer, PAR Direct, UK), parafilm, and a metal clamp. Graphite felt materials typically used in RFB cells (Sigracell GFD 4.6 EA, SGL Carbon, Germany) were used as electrodes, with titanium rods threaded through as current-collecting wires. Cyclic voltammograms of both

negolyte (Figure S16a, Supporting Information) and posolyte (Figure S16b, Supporting Information) 10 mM solutions (with 100 mM TBAP supporting electrolyte) were performed in a three-electrode set-up and calibrated against a ferrocene standard to estimate OCV. Subsequently, a four-electrode set-up was used, with positive electrode current and voltage sense connected to the TEMPO solution, and the negative electrode current and voltage sense connected to the metal ionic liquid solution. In this case, a 15 mL 100 mM $[C_4py][FeCl_4]$ in MeCN solution was used as the negolyte, and a 15 mL 100 mM TEMPO in MeCN solution for the posolyte, allowing for both solutions to be soaked into the porous graphite felt before testing. Galvanostatic charge-discharge cycling at +/-4 mA was conducted using the same potentiostat as used for cyclic voltammetry, with upper and lower cut-off voltages of 1.20 and 0.05 V, respectively.

Supporting Information

Supporting Information is available from the Wiley Online Library or from the author.

Acknowledgements

C.B. and B.B. contributed equally to this work. The authors thank A. Nitschke (Univ. Potsdam) for her involvement in TGA, S. Mies (Univ. Potsdam) for his help with DSC, A. Lange (Univ. Potsdam) for her valuable input in CV discussions. The authors also thank Prof. Dr. M. Swadźba-Kwaśny (QUILL) for her helpful input in the overall project and Dr. M. Drüschler (rhd) for his expertise and kind help with cyclic voltammetry. The author also greatly appreciates the input of Dr. A. Holländer (FH IAP) regarding the XPS analysis. Funding from the University of Potsdam (grant #53170000) and the Leistungszentrum Funktionsintegration is gratefully acknowledged.

Open access funding enabled and organized by Projekt DEAL.

Conflict of Interest

The authors declare no conflict of interest.

Data Availability Statement

The data that support the findings of this study are available from the corresponding author upon reasonable request.

Keywords

chloridoferrate(III), Ionic liquids, redox flow battery

Received: September 22, 2023
Revised: October 27, 2023
Published online: December 14, 2023

[1] J. P. Hallett, T. Welton, *Chem. Rev.* **2011**, *111*, 3508.
[2] M. Watanabe, M. L. Thomas, S. Zhang, K. Ueno, T. Yasuda, K. Dokko, *Chem. Rev.* **2017**, *117*, 7190.
[3] J. Salgado-Beceiro, J. M. Bermúdez-García, A. L. Llamas-Saiz, S. Castro-García, M. A. Señarís-Rodríguez, F. Rivadulla, M. Sánchez-Andújar, *J. Mater. Chem. C* **2020**, *8*, 13686.
[4] D. V. Chernyshov, V. M. Egorov, N. V. Shvedene, I. V. Pletnev, *ACS Appl. Mater. Interfaces* **2009**, *1*, 2055.
[5] Y. Gu, G. Li, *Adv. Synth. Catal.* **2009**, *351*, 817.
[6] D. S. Silvester, *Analyst* **2011**, *136*, 4871.
[7] T. Yamamoto, T. Nohira, *Chem. Rec.* **2023**, *202300169*, 1.
[8] O. M. Leung, T. Schoetz, T. Prodromakis, C. Ponce De Leon, *J. Electrochem. Soc.* **2021**, *168*, 056509.
[9] A. R. Ubbelohde, H. J. Michels, J. J. Duruz, *Nature* **1970**, *228*, 50.
[10] H. Abe, *J. Mol. Liq.* **2021**, *332*, 115189.
[11] J. Sun, J. Wu, X. Tong, F. Lin, Y. Wang, Z. M. Wang, *Adv. Sci.* **2018**, *5*, 1700780.
[12] Y.-H. Kim, H. Cho, T.-W. Lee, *Proc. Natl. Acad. Sci. USA* **2016**, *113*, 11694.
[13] C. Balischewski, B. Bhattacharyya, E. Sperlich, C. Günter, A. Beqiraj, T. Klamroth, K. Behrens, S. Mies, A. Kelling, S. Lubahn, L. Holtzheimer, A. Nitschke, A. Taubert, *Chem.A Eur. J.* **2022**, *28*, e202201068.
[14] C. Balischewski, K. Behrens, K. Zehbe, C. Guenter, S. Mies, E. Sperlich, A. Taubert, A. Kelling, *Chem.A Eur. J.* **2020**, *26*, 17504.
[15] K. Behrens, C. Balischewski, E. Sperlich, A. Menski, R. F. Balderas-Valadez, C. Pacholski, C. Günter, S. Lubahn, A. Kelling, A. Taubert, *RSC Adv.* **2022**, *12*, 35072.
[16] B. Bhattacharyya, C. Balischewski, E. Sperlich, C. Günter, S. Mies, A. Kelling, A. Taubert, *Adv. Mater. Interfaces* **2023**, *10*, 1.
[17] M. Currie, J. Estager, P. Licence, S. Men, P. Nockemann, K. R. Seddon, M. Swadzba-Kwasny, C. Terrade, *Inorg. Chem.* **2013**, *52*, 1710.
[18] S. J. Osborne, S. Wellens, C. Ward, S. Felton, R. M. Bowman, K. Binnemans, M. Swadźba-Kwäny, H. Q. Nimal Gunaratne, P. Nockemann, *Dalt. Trans.* **2015**, *44*, 11286.
[19] P. Nockemann, B. Thijs, N. Postelmans, K. Van Hecke, L. Van Meervelt, K. Binnemans, *J. Am. Chem. Soc.* **2006**, *128*, 13658.
[20] J. Estager, P. Nockemann, K. R. Seddon, M. Swadzba-Kwasny, S. Tyrrell, *Inorg. Chem.* **2011**, *50*, 5258.
[21] D. Prodius, F. Macaev, E. Stingaci, V. Pogrebnoi, V. Mereacre, G. Novitchi, G. E. Kostakis, C. E. Anson, A. K. Powell, *Chem. Commun.* **2013**, *49*, 2628.
[22] I. J. Bruno, J. C. Cole, P. R. Edgington, M. Kessler, C. F. Macrae, P. Mccabe, J. Pearson, R. Taylor, *Acta Crystallogr* **2002**, *58*, 389.
[23] R. Fernández, J. Gutierrez, A. Eceiza, A. Tercjak, *RSC Adv.* **2015**, *5*, 15740.
[24] D. Wyrzykowski, R. Kruszyn´Ski, J. Klak, J. Mrozin´Ski, Z. Warnke, *Inorganica. Chim. Acta.* **2008**, *361*, 262.
[25] H. C. Freeman, G. H. W. Milburn, C. E. Nockolds, P. Hemmerich, K. H. Knauer, *J. Chem. Soc. D* **1969**, *55*, 886.
[26] T. Morawitz, H. W. Lerner, M. Bolte, *Acta Crystallogr* **2007**, *63*, 7.
[27] S. Rana, J. P. Biswas, A. Sen, M. Clémancey, G. Blondin, J.-M. Latour, G. Rajaraman, D. Maiti, *Chem. Sci.* **2018**, *9*, 7843.
[28] Y. Gao, J. Guery, C. Jacoboni, *Acta Crystallogr* **1993**, *49*, 147.
[29] P. González-Izquierdo, O. Fabelo, G. Beobide, O. Vallcorba, F. Sce, J. Rodríguez Fernández, M. T. Fernández-Díaz, I. De Pedro, *Inorg. Chem.* **2018**, *57*, 1787.
[30] B. M. Krieger, H. Y. Lee, T. J. Emge, J. F. Wishart, E. W. Castner Jr., *Phys. Chem. Chem. Phys.* **2010**, *12*, 8919.
[31] C. D. Wagner, L. E. Davis, M. V. Zeller, J. A. Taylor, R. H. Raymond, L. H. Gale, *Surf. Interface Anal.* **1981**, *3*, 211.
[32] S. Men, P. Licence, H. Luo, S. Dai, *J. Phys. Chem. B* **2020**, *124*, 6657.
[33] I. J. Villar-Garcia, E. F. Smith, A. W. Taylor, F. Qiu, K. R. J. Lovelock, R. G. Jones, P. Licence, *Phys. Chem. Chem. Phys.* **2011**, *13*, 2797.
[34] S. Men, D. S. Mitchell, K. R. J. Lovelock, P. Licence, *ChemPhysChem* **2015**, *16*, 2211.
[35] G. Beamson, D. Briggs, *Mol. Phys.* **1992**, *76*, 919.
[36] N. Calisi, S. Martinuzzi, A. Giaccherini, C. S. Pomelli, L. Guazzelli, S. Caporali, *J. Electron. Spectros. Relat. Phenomena.* **2021**, *247*, 147034.
[37] D. Nava, I. González, D. Leinen, J. R. Ramos-Barrado, *Electrochim. Acta* **2008**, *53*, 4889.

[38] W. Zhu, P. Wu, L. Yang, Y. Chang, Y. Chao, H. Li, Y. Jiang, W. Jiang, S. Xun, *Chem. Eng. J.* **2013**, *229*, 250.
[39] K. Ben Brahim, M. Ben Gzaiel, A. Oueslati, K. Khirouni, M. Gargouri, G. Corbel, J.-F. Bardeau, *RSC Adv.* **2021**, *11*, 18651.
[40] T. Bäcker, O. Breunig, M. Valldor, K. Merz, V. Vasylyeva, A.-V. Mudring, *Cryst. Growth Des.* **2011**, *11*, 2564.
[41] C. Martin, I. Cano, F. Scé, R. Pérez-Aguirre, C. Gimbert-Suriñach, P. Lopez-Cornejo, I. De Pedro, *New J. Chem.* **2020**, *44*, 6375.
[42] J. Wang, H. Yao, Y. Nie, X. Zhang, J. Li, *J. Mol. Liq.* **2012**, *169*, 152.
[43] K. Bica, S. Leder, P. Gaertner, *Curr. Org. Synth.* **2011**, *8*, 824.
[44] M. Valvo, A. Liivat, H. Eriksson, C.-W. Tai, K. Edström, *ChemSusChem* **2017**, *10*, 2431.
[45] Y. Zhao, Y. Zhen, T. Boström, *ACS Omega* **2022**, *7*, 24082.
[46] I. Iwakiri, T. Antunes, H. Almeida, J. P. Sousa, R. B. Figueira, A. Mendes, *Energies* **2021**, *14*, 5643.
[47] Z. Li, Y.-C. Lu, *Chem* **2018**, *4*, 2020.
[48] H. Zhang, C. Sun, M. Ge, *Batteries* **2022**, *8*, 202.
[49] S. Yu, X. Yue, J. Holoubek, X. Xing, E. Pan, T. Pascal, P. Liu, *J. Power Sources* **2021**, *513*, 230457.
[50] K. Gong, X. Ma, K. M. Conforti, K. J. Kuttler, J. B. Grunewald, K. L. Yeager, M. Z. Bazant, S. Gu, Y. Yan, *Energy Environ. Sci.* **2015**, *8*, 2941.
[51] L. W. Hruska, R. F. Savinell, *J. Electrochem. Soc.* **1981**, *128*, 18.
[52] J. G. Ibanez, C.-S. Choi, R. S. Becker, *J. Electrochem. Soc.* **1987**, *134*, 3083.
[53] C.-N. Sun, F. Delnick, L. Baggetto, G. M. Veith, T. A. Zawodzinski, *ECS Meet. Abstr.* **2013**, *MA2013-02*, 1665.
[54] P. Schröder, D. Obendorf, T. Bechtold, *ChemElectroChem* **2019**, *6*, 3311.
[55] Y. H. Wen, H. M. Zhang, P. Qian, H. T. Zhou, P. Zhao, B. L. Yi, Y. S. Yang, *J. Electrochem. Soc.* **2006**, *153*, A929.
[56] N. Arroyo-Currás, J. W. Hall, J. E. Dick, R. A. Jones, A. J. Bard, *J. Electrochem. Soc.* **2015**, *162*, A378.
[57] C. Noh, Y. Chung, Y. Kwon, *J. Power Sources* **2020**, *466*, 228333.
[58] C. Noh, Y. Chung, Y. Kwon, *Chem. Eng. J.* **2021**, *405*, 126966.
[59] C. Noh, Y. Chung, Y. Kwon, *J. Power Sources* **2021**, *495*, 229799.
[60] M. H. Chakrabarti, R. A. W. Dryfe, E. P. L. Roberts, *Electrochim. Acta* **2007**, *52*, 2189.
[61] Y. H. Wen, H. M. Zhang, P. Qian, H. T. Zhou, P. Zhao, B. L. Yi, Y. S. Yang, *Electrochim. Acta* **2006**, *51*, 3769.
[62] K. Gong, F. Xu, J. B. Grunewald, X. Ma, Y. Zhao, S. Gu, Y. Yan, *ACS Energy Lett.* **2016**, *1*, 89.
[63] A. Lê, D. Floner, T. Roisnel, O. Cador, L. Chancelier, F. Geneste, *Electrochim. Acta* **2019**, *301*, 472.
[64] S. Sreenath, N. K. Sharma, R. K. Nagarale, *RSC Adv.* **2020**, *10*, 44824.
[65] M. Shin, C. Noh, Y. Chung, Y. Kwon, *Chem. Eng. J.* **2020**, *398*, 125631.
[66] M. Shin, S. Oh, H. Jeong, C. Noh, Y. Chung, J. W. Han, Y. Kwon, *Int. J. Energy Res.* **2022**, *46*, 8175.
[67] M. Shin, C. Noh, Y. Kwon, *Chem. Eng. J.* **2023**, *453*, 139738.
[68] P. Schröder, N. Aguiló-Aguayo, D. Obendorf, T. Bechtold, *Electrochim. Acta* **2022**, *430*, 141042.
[69] C. L. Staiger, H. D. Pratt III, J. C. Leonard, D. Ingersoll, T. M. Anderson, MetILs: A FAMILY OF METAL IONIC LIQUIDS FOR REDOX FLOW BATTERIES, October **2011**.
[70] F. Neve, A. Crispini, S. Armentano, O. Francescangeli, *Chem. Mater.* **1998**, *10*, 1904.
[71] Z. Guo, T. Zhang, M. Khan, S. Gao, T. Liu, J. Yu, *Electrochim. Acta* **2014**, *142*, 132.
[72] S. R. Belding, J. G. Limon-Petersen, E. J. F. Dickinson, R. G. Compton, *Angew. Chemie. Int. Ed.* **2010**, *49*, 9242.
[73] N. Elgrishi, K. J. Rountree, B. D. Mccarthy, E. S. Rountree, T. T. Eisenhart, J. L. Dempsey, *J. Chem. Educ.* **2018**, *95*, 197.
[74] M. Yamagata, N. Tachikawa, Y. Katayama, T. Miura, *Electrochim. Acta* **2007**, *52*, 3317.
[75] C. Sandford, M. A. Edwards, K. J. Klunder, D. P. Hickey, M. Li, K. Barman, M. S. Sigman, H. S. White, S. D. Minteer, *Chem. Sci.* **2019**, *10*, 6404.
[76] J.-M. Savéant, *ACS Catal.* **2018**, *8*, 7608.
[77] O. A. González-Meza, E. R. Larios-Durán, A. Gutiérrez-Becerra, N. Casillas, J. I. Escalante, M. Bárcena-Soto, *J. Solid State Electrochem.* **2019**, *23*, 3123.
[78] J. B. Gerken, S. S. Stahl, *ACS Cent. Sci.* **2015**, *1*, 234.
[79] M. A. Miller, J. S. Wainright, R. F. Savinell, *J. Electrochem. Soc.* **2017**, *164*, A796.
[80] S.-H. Shin, S.-H. Yun, S.-H. Moon, *RSC Adv.* **2013**, *3*, 9095.
[81] M. Li, S. A. Odom, A. R. Pancoast, L. A. Robertson, T. P. Vaid, G. Agarwal, H. A. Doan, Y. Wang, T. M. Suduwella, S. R. Bheemireddy, R. H. Ewoldt, R. S. Assary, L. Zhang, M. S. Sigman, S. D. Minteer, *ACS Energy Lett.* **2021**, *6*, 3932.
[82] G. M. Sheldrick, *Acta Crystallogr.* **2015**, *71*, 3.
[83] G. M. Sheldrick, *Acta Crystallogr.* **2008**, *64*, 112.
[84] K. Brandenburg, H. Putz, *Diamond–Crystal and Molecur Structure Visualization*, Crystal Impact Diamond, Bonn, Germany **2020**.